On Theoretical Broadband Shock-Associated Noise Near-Field Cross-Spectra

Steven A. E. Miller*

The National Aeronautics and Space Administration

The cross-spectral acoustic analogy is used to predict auto-spectra and cross-spectra of broadband shock-associated noise in the near-field and far-field from a range of heated and unheated supersonic off-design jets. A single equivalent source model is proposed for the near-field, mid-field, and far-field terms, that contains flow-field statistics of the shock wave shear layer interactions. Flow-field statistics are modeled based upon experimental observation and computational fluid dynamics solutions. An axisymmetric assumption is used to reduce the model to a closed-form equation involving a double summation over the equivalent source at each shock wave shear layer interaction. Predictions are compared with a wide variety of measurements at numerous jet Mach numbers and temperature ratios from multiple facilities. Auto-spectral predictions of broadband shock-associated noise in the near-field and far-field capture trends observed in measurement and other prediction theories. Predictions of spatial coherence of broadband shock-associated noise accurately capture the peak coherent intensity, frequency, and spectral width.

Nomenclature

Symbols	Description
A_{ijlm}	Coefficient matrix
D	Nozzle exit diameter
D_j	Fully-expanded diameter
c	Speed of sound
F_t	Far-field term
f_i	Equivalent source term
G	Cross-power spectral density
I	Modified Bessel function
k	Turbulent kinetic energy
l_c	Turbulent length scale coefficient
l_i	Turbulent length scale
M_d	Design Mach number
M_t	Mid-field term
M_j	Fully-expanded Mach number
N_s	Number of shocks
N_t	Near-field term
P_f	Constant
p	Pressure
p_s	Shock pressure
p_t	Total pressure
R	Gas constant or radiation distance
R_{mn}	Two-point cross-correlation
R^v_{ijlm}	Two-point cross-correlation of source
S_i	Shock wave thickness
St	Strouhal number
$\boldsymbol{r}$	Radiation vector
T	Temperature
T_j	Fully-expanded temperature
T_{ij}	Lighthill stress tensor
$\boldsymbol{u}$	Velocity vector
u_c	Convection velocity
u_j	Fully-expanded jet velocity
$\boldsymbol{x}$	Observer vector
$\boldsymbol{y}$	Source vector
y_c	Jet core length
z	Radial cylindrical coordinate
α_i	Constant
β	Off-design parameter
Γ	Coherence
γ	Ratio of specific heats
Δ	Separation operator
$\boldsymbol{\eta}(\xi,\eta,\zeta)$	Source separation vector
ρ	Density
θ_i	Observer angle relative to downstream nozzle axis
ϕ_i	Azimuthal cylindrical coordinate
Ψ	Observer angle relative to upstream nozzle axis
τ	Retarded time
τ_c	Turbulent time scale coefficient
τ_s	Turbulent time scale
ω	Radial frequency
$\tilde{\omega}$	Modified radial frequency

Abbreviations	
BBSAN	Broadband shock-associated noise
CPSD	Cross-power spectral density
PSD	Power spectral density
RANS	Reynolds-averaged Navier-Stokes
SHJAR	Small Hot Jet Acoustic Rig
TTR	Total temperature ratio

*Research Aerospace Engineer, Aeroacoustics Branch, NASA Langley Research Center, 2 N. Dryden St. MS 461, Hampton, VA, 23681, USA, AIAA Senior Member, s.miller@nasa.gov

Introduction

The interaction of high speed convecting turbulence with a shock wave results in high intensity acoustic radiation. This radiation is broadband in nature, and it is dependent on the convection velocity and intensity of the turbulence, and strength of the shock wave. Systems of shock waves are present within off-design supersonic turbulent jets. Off-design supersonic jets are created by propulsion systems of flight vehicles that include rockets, missiles, aircraft, and by some natural phenomenon. Coherent turbulence in the jet shear layer interacts with the shock cells and produces broadband shock-associated noise (BBSAN). The radiation from subsequent shock wave shear layer interactions combines constructively and is characterized by multiple broad spectral lobes. This radiation may impinge on the flight vehicle and can also cause observer hearing loss or annoyance. Predicting the cross-power spectral density (CPSD) of BBSAN is beneficial for understanding the physics of the radiating source and also provides mathematical guidance for flight vehicle designers. This paper presents an approach to predict the near-field intensity and coherence of off-design supersonic jets using the cross-spectral acoustic analogy.

In the far-field BBSAN is dominant at mid- to high- frequencies in the upstream and sideline direction relative to the jet flow. Generally, BBSAN is dominated by other noise components in the downstream direction. Harper-Bourne and Fisher[1] proposed that the intensity of BBSAN increases as β^4, where β is the off-design parameter involving the fully-expanded Mach number, M_j, and design Mach number, M_d. A general form of the off-design parameter is, $\beta = |M_j^2 - M_d^2|^{1/2}$. Norum and Seiner[2] showed that the β^4 relationship is invalid when Mach disks form within the jet plume with increasing nozzle pressure ratio (NPR). Generally, the intensity scaling of BBSAN is strongly dependent on NPR and very weakly dependent on total temperature ratio (TTR). Viswanathan et al.[3] noted that when NPR is held constant and TTR increases the BBSAN intensity saturates (ceases to increase). A physical explanation for the saturation of BBSAN was proposed by Miller.[4] The source of BBSAN is the interaction of large-scale coherent turbulence within the jet shear layer interacting with the shock waves. Each of these shock wave shear layer interactions creates outgoing acoustic waves. As the waves propagate from the near-field to the far-field, they constructively interfere to form characteristic broad lobes in the far-field. BBSAN spectra are characterized by multiple broad lobes that decrease in intensity with increasing frequency. Though this noise component is broadband and random, it is highly coherent near peak frequencies due to its constructive nature, and almost entirely incoherent at relatively low and high frequencies. The spatial coherence of BBSAN decreases with increasing observer separation distance and increasing frequency.

A number of experiments were conducted to study the noise from off-design jets. Early measurements of Yu[5] yielded contour plots of BBSAN intensity in the jet near-field. Soon after, Tanna[6] measured far-field auto-spectra for a wide range of jet Mach numbers and temperature ratios from convergent nozzles, and isolated the BBSAN component of the spectrum using the prediction method of Harper-Bourne and Fisher.[1] Tam and Tanna[7] defined β to account for convergent-divergent nozzles and jet stagnation temperature variation. The same year that Tam and Tanna[7] presented their work, Norum and Seiner[2] examined the variation of peak Helmholtz number of BBSAN relative to unheated jets from a convergent nozzle. Norum and Seiner[2] used a near-field microphone array to characterize BBSAN intensity and their results agreed with the early findings of Yu.[5] Seiner and Yu[8] used a near-field linear microphone array located 2.68 jet diameters from the nozzle centerline to confirm measurements of Harper-Bourne and Fisher,[1] who showed that the shock-associated noise intensity is proportional to the first power of the fluctuating velocity components within the jet mixing layer.

Bridges and Brown[9] and Bridges and Wernet[10] examined far-field auto-spectra and performed time resolved particle image velocimetry from a large range of off-design jets. Turbulent statistics along the nozzle lip line were shown to possess some similarity for on-design jets. For off-design jets, the similarity is not readily apparent because of the large gradients of turbulent kinetic energy (k) (and other turbulence statistics) after each shock wave shear layer interaction. The far-field auto-spectral and turbulence measurements of Bridges and Brown[9] and Bridges and Wernet[10] are an important part of the present model development. These increases in turbulent kinetic energy are complicated by oscillations of the shock waves (as described by Panda[11]) and cause a noticeable effect of broadening the spectrum of BBSAN in the far-field.

Recently, Viswanathan et al.[3] isolated the BBSAN component of jet noise incoherently, like Tanna,[6] but used the theory of fine- and large-scale similarity spectral subtraction. They observed nonlinear propagation of BBSAN, the saturation of BBSAN with increasing temperature, and most importantly the decay of coherence between observer pairs. A similar investigation of Kuo et al.,[12] using helium-air mixtures to simulate jet heating, showed that BBSAN saturates with increasing temperature. Savarese et al.[13] made

measurements within the jet near-field for multiple pressure ratios. Significant coherence was observed between fluctuating velocity quantities at the shock wave shear layer interactions and the acoustic field. Savarese et al.[13] also examined flight vehicle Mach number effects and their measurements were in agreement with Norum and Shearin[14] and Ahuja et al.[15]

Many mathematical models were developed to predict BBSAN, and here we survey those without significant empiricism. Harper-Bourne and Fisher[1] created the first successful prediction methodology for BBSAN that depends on the rate of decay of turbulence between shocks and a characteristic spectrum produced by each shock wave shear layer interaction. The model was based on the premise of coherent interaction between turbulence in the jet shear layer and the nearly periodic jet shock cell structure. More recently, Harper-Bourne[16] created a prediction technique for the near-field intensity of jet mixing noise and BBSAN. This near-field model for BBSAN intensity depends on a master spectrum, which is like the model of Harper-Bourne and Fisher.[1]

Tam et al.,[17] based on the preliminary work of Tam and Jackson,[18] developed a linear multiple scales model of the shock-cell structure. This model, which is more physical than the model of Pack,[19] takes into account the gradual spatial change of the jet spreading and the smoothing of gradients by turbulence. The effect of divergence and turbulent dissipation was included following the method of Tam et al.[17] Tam[20] developed a stochastic model for BBSAN where the basic physical model was described by Tam and Tanna.[7] The large-scale turbulence in the jet shear layer was modeled as a random superposition of instability waves supported by the jet mean flow, as described by Tam and Chen.[21] Tam[22] modified the model of Tam[20] to predict BBSAN from heated jets with a moderate off-design parameter. The stochastic model of Tam[20] was shown to predict near-field BBSAN intensity and compared very favorably with the measurements of Yu.[5]

Morris and Miller[23] developed a prediction method for BBSAN that is based upon an acoustic analogy approach. The Euler equations were rearranged into the linearized Euler equations (LEE) operator and were equated to equivalent sources. The resultant model consisted of a volume integral containing the jet plume and an integral of the shock cell pressure wavenumber spectrum. Their acoustic analogy successfully predicted BBSAN for a wide range of jet operating conditions. Miller and Morris[24] studied propagation of BBSAN by altering the vector Green's function of the LEE to contain the Green's function of Lilley's equation as an argument. It was shown that in the upstream and sideline radiation direction, refraction effects have little impact on BBSAN. Very recently, Miller[25] created an acoustic analogy for jet noise that included equivalent sources for both turbulent mixing noise and BBSAN, that was shown to predict the total noise accurately for a wide range of jet Mach numbers and jet stagnation temperatures.

The models of Harper-Bourne and Fisher,[1] Harper-Bourne,[16] Tam,[20] or Miller[25] are very good at predicting the power spectral density in the far-field; however, they are not capable of predicting cross-power spectral density in the near-field. Recently, the cross-spectral acoustic analogy was developed by Miller[26] to overcome similar difficulties present within other problems of interest to NASA. It can be shown that the cross-spectral acoustic analogy can be simplified to produce Lighthill's[27,28] acoustic analogy when both observers are in the far-field and at the same location.

In this paper we formulate a model for the CPSD of BBSAN based upon the cross-spectral acoustic analogy of Miller.[26] A source term is proposed for the two-point cross-correlation of the Lighthill stress tensor and is valid for a wide range of jet operating conditions. Arguments of the source term are dependent on the jet Mach number and jet temperature, among other terms. The scaling of the source model is formulated based upon the work of Morris and Miller[23] but in the framework of Lighthill's acoustic analogy. Anisotropic effects of the source are partially taken into account through arguments of the observer vectors and varying turbulent scales. Spatial integration of the shock wave shear layer interactions are performed analytically by assuming that the jet flow-field is axisymmetric. The resulting closed-form model for the CPSD of BBSAN in the near-field involves a double summation of the source at all shock wave shear layer interactions.

The next section of this paper presents a mathematical model for the prediction of the CPSD of BBSAN. Arguments of the CPSD BBSAN model are defined in relation to the jet Mach number and temperature. Predictions are presented for far-field and near-field BBSAN intensity and BBSAN spatial coherence and are compared with measurement. Finally, a summary and conclusion closes the paper.

Mathematical Theory

We assume that the Navier-Stokes equations model the physics of shock wave shear layer interactions and subsequent sound production and propagation. A partial derivative operator with respect to time and a divergence operator are applied to the continuity and momentum equations respectively. The difference of the resulting equations are added to a wave equation operator with mixed independent values of pressure and density. The resultant equation contains the well known Lighthill stress tensor, T_{ij} (see Lighthill[27] for details and discussion of T_{ij}). The right hand side of this equation represents an equivalent aerodynamic source of sound. We expand the first and second terms of the right hand side, and unlike Lighthill,[27] we retain all terms. A vector free stream Mach number is introduced to account for source convection, density is converted to pressure, and the result is written more compactly. The resulting equation for pressure is used to form a cross-correlation between two observer points $\boldsymbol{x}_1$ and $\boldsymbol{x}_2$. The theories of Lighthill,[29,27] Ribner,[30] and Ffowcs Williams[31] are used to simplify the resulting spatial cross-correlation for pressure using the assumption that the turbulence is statistically stationary. We then group integrand terms according to their relative contribution to the near-field, mid-field, and far-field. Terms with second order powers in propagation correspond to far-field terms, fourth order powers correspond to the mid-field terms, and sixth order powers correspond to near-field terms. The CPSD is then found using a forward transform. We find the cross-spectral acoustic analogy of Miller[26]

$$G\left(\boldsymbol{x}_1,\boldsymbol{x}_2,\omega\right)=\frac{1}{16\pi^2}\int_{-\infty}^{\infty}\ldots\int_{-\infty}^{\infty}\left\{\overbrace{F_t\overline{\ddot{T}_{ij}\ddot{T}'_{lm}}}^{\text{Far-Field Term}}+\overbrace{M_t\overline{\dot{T}_{ij}\dot{T}'_{lm}}}^{\text{Mid-Field Term}}+\overbrace{N_t\overline{T_{ij}T'_{lm}}}^{\text{Near-Field Term}}\right\}\times\exp\left[-i\omega\left(\tau+\frac{r_1}{c_\infty}-\frac{r_2}{c_\infty}\right)\right]d\tau d\boldsymbol{y}_2 d\boldsymbol{y}_1, \tag{1}$$

where c is the speed of sound, G is the cross-power spectral density, $\boldsymbol{x}_1$ and $\boldsymbol{x}_2$ are vectors from the origin to observers, $\boldsymbol{y}_1$ and $\boldsymbol{y}_2$ are vectors from the origin to source positions, τ is the retarded time, and ω is the radial frequency. Vectors $\boldsymbol{r}_1$ and $\boldsymbol{r}_2$ are defined from each source position to each observer. The primes denote quantities at position $\boldsymbol{y}_2$. Evaluation of Eqn. 1 yields the CPSD due to a convecting turbulent field within a free-stream Mach number, $\boldsymbol{M}_\infty$, and its application is not limited to jet flows. Note that the propagation operator of the cross-spectral acoustic analogy is the three-dimensional wave equation operator. Two-point cross-correlations involving various retarded time derivatives of the Lighthill stress tensor, T_{ij}, appear before various terms. Prefactor terms, F_t, M_t, and N_t, involve directional trigonometric functions that correspond to the far-field, mid-field, and near-field. For example

$$F_t=\frac{r_i r_j r'_l r'_m}{r^2 r'^2}\left[\frac{1}{c_\infty^4 r r'}\right] \tag{2}$$

and M_t and N_t are shown by Miller,[26] and are not repeated here for compactness. To evaluate Eqn. 1 knowledge of $\overline{T_{ij}T'_{lm}}$ and its derivatives must be known. In particular, for out-going acoustic radiation we must model $\overline{\ddot{T}_{ij}\ddot{T}'_{lm}}$ and note the relation

$$\overline{\ddot{T}_{ij}\ddot{T}'_{lm}}=\frac{\partial^4}{\partial\tau^4}R^v_{ijlm}(\boldsymbol{y}_1,\boldsymbol{\eta},\tau), \tag{3}$$

where $\boldsymbol{\eta}=\boldsymbol{\eta}(\xi,\eta,\zeta)$ is a vector between source positions $\boldsymbol{y}_1$ and $\boldsymbol{y}_2$.

We must now model $R^v_{ijlm}(\boldsymbol{y}_1,\boldsymbol{\eta},\tau)$, and the model should characterize the BBSAN equivalent source. As there is no basis for an equivalent source for BBSAN in the context of a Lighthill acoustic analogy, we pause and reexamine the model of Morris and Miller[23] who developed a similar relation. The model of Morris and Miller[23] is developed for an acoustic analogy based on the linearized Euler equations. Their two-point cross-correlation of the right hand side source terms that characterize BBSAN is defined as

$$R^v_{mn}=\overline{f^v_n(\boldsymbol{y}_1,t)f^v_m(\boldsymbol{y}_1+\boldsymbol{\eta},t+\tau)}, \tag{4}$$

where

$$f^v_i=-u_{s,j}\frac{\partial u_{t,i}}{\partial x_j}-u_{t,j}\frac{\partial u_{s,i}}{\partial x_j} \tag{5}$$

and u_s and u_t involve unsteady velocity components due to the shocks and turbulence respectively. The term f_i^v is present on the right hand side of the acoustic analogy shown in Morris and Miller.[23] Morris and Miller[23] proposed a model for the two-point cross-correlation of f_i^v as

$$R_{mn}^v = \frac{p_s p_{s,\eta} k}{\rho_\infty^2 c_\infty^2 l_s^2} \exp\left[-\frac{|\tau|}{\tau_s}\right] \exp\left[-\frac{(\xi - u_c \overline{u}\tau)^2}{l_s^2}\right] \exp\left[-\frac{(\eta^2 + \zeta^2)}{l_\perp^2}\right], \tag{6}$$

where k is the turbulent kinetic energy, p_s is the shock pressure, l_s and $l_\perp$ are streamwise and cross-stream turbulent length scales, $\overline{u}$ is the time-averaged streamwise velocity component, and τ_s is the turbulent time scale. Note that the subscript η denotes that the quantity is evaluated at $\boldsymbol{y}_1 + \boldsymbol{\eta}$. Scales of turbulence vary spatially within the turbulent field, and can be approximated numerically with a steady Reynolds-averaged Navier-Stokes (RANS) solution, unsteady numerical methods, or with simpler models (that will be discussed below). Vector components of $\boldsymbol{\eta}$ are ξ, η, and ζ respectively.

Based on the model of Morris and Miller,[23] which was developed for the LEE operator and its associated equivalent sources, we propose an equivalent source for BBSAN

$$R_{ijlm}^v = \frac{A_{ijlm}}{\pi^{1/2} \tau_s^4 \omega^4} \frac{p_s p_{s,\eta}}{c^2} R_{ijlm}, \tag{7}$$

where

$$R_{ijlm} = k \exp\left[\frac{-|\xi|}{\overline{u}\tau_s}\right] \exp\left[\frac{-(\xi - \overline{u}\tau)^2}{l_s^2}\right] \exp\left[\frac{-\eta^2}{l_{sy}^2}\right] \exp\left[\frac{-\zeta^2}{l_{sz}^2}\right], \tag{8}$$

A_{ijlm} is a coefficient matrix that describes anisotropic effects, and subscripts y and z denote cross-stream scales in radial directions. The terms chosen within Eqn. 8 are Guassian and model two-point cross-correlation measurements of velocity fluctuations within turbulent flows. Relatively more complicated forms or empirical fits can be chosen, but these choices do not yield large increases in prediction accuracy and prevent the ease of analytical integration. We scale the two-point cross-correlation with the local k. The terms of Eqn. 7 are chosen based on the model for turbulent mixing noise (see Miller[26]) and Eqn. 4. BBSAN intensity scales with NPR and TTR as approximately $p_s^2 k$, and for normalization and TTR saturation purposes is multiplied by c^{-2}. The scaling of BBSAN intensity using this equivalent source model compares favorably with β^4. In summary this choice of R_{ijlm}^v is consistent with the model of Morris and Miller[23] and Harper-Bourne and Fisher,[1] in that the scaling is consistent with their predictions and associated measurements, respectively.

By examining the far-field, mid-field, and near-field terms of Eqn. 1, it is apparent that Eqn. 7 must be differentiated with respect to τ multiple times, multiplied by an exponential factor involving τ, and finally integrated with respect with τ. These operations for the near-field term result in

$$\begin{aligned} &\int_{-\infty}^{\infty} \frac{A_{ijlm}}{\pi^{1/2} \tau_s^4 \omega^4} \frac{p_s p_{s,\eta} k}{c^2} \exp\left[\frac{-|\xi|}{\overline{u}\tau_s}\right] \exp\left[\frac{-(\xi - \overline{u}\tau)^2}{l_s^2}\right] \exp\left[\frac{-\eta^2}{l_{sy}^2}\right] \exp\left[\frac{-\zeta^2}{l_{sz}^2}\right] \exp\left[-i\omega\tau\right] d\tau \\ &\qquad = \frac{A_{ijlm}}{\tau_s^4 \omega^4} \frac{p_s p_{s,\eta} k}{c^2} \frac{l_s}{\overline{u}} \exp\left[\frac{-|\xi|}{\overline{u}\tau_s}\right] \exp\left[\frac{-\eta^2}{l_{sy}^2}\right] \exp\left[\frac{-\zeta^2}{l_{sz}^2}\right] \exp\left[-\frac{\omega\left(4i\overline{u}\xi + l_s^2\omega\right)}{4\overline{u}^2}\right] \end{aligned} \tag{9}$$

and for the mid-field

$$\begin{aligned} &\int_{-\infty}^{\infty} \frac{\partial^2}{\partial\tau^2} \left\{ \frac{A_{ijlm}}{\pi^{1/2} \tau_s^4 \omega^4} \frac{p_s p_{s,\eta} k}{c^2} \exp\left[\frac{-|\xi|}{\overline{u}\tau_s}\right] \exp\left[\frac{-(\xi - \overline{u}\tau)^2}{l_s^2}\right] \exp\left[\frac{-\eta^2}{l_{sy}^2}\right] \exp\left[\frac{-\zeta^2}{l_{sz}^2}\right] \right\} \exp\left[-i\omega\tau\right] d\tau \\ &\qquad = \int_{-\infty}^{\infty} \frac{A_{ijlm}}{\pi^{1/2} \tau_s^4 \omega^4} \frac{p_s p_{s,\eta} k}{c^2} \exp\left[\frac{-|\xi|}{\overline{u}\tau_s}\right] \frac{-2\overline{u}^2\left(l_s^2 - 2(\xi - \overline{u})^2\right)}{l_s^4} \exp\left[\frac{-(\xi - \overline{u}\tau)^2}{l_s^2}\right] \\ &\qquad\qquad \times \exp\left[\frac{-\eta^2}{l_{sy}^2}\right] \exp\left[\frac{-\zeta^2}{l_{sz}^2}\right] \exp\left[-i\omega\tau\right] d\tau \\ &\qquad = \frac{A_{ijlm}}{\tau_s^4 \omega^2} \frac{p_s p_{s,\eta} k}{c^2} \frac{l_s}{\overline{u}} \exp\left[\frac{-|\xi|}{\overline{u}\tau_s}\right] \exp\left[\frac{-\eta^2}{l_{sy}^2}\right] \exp\left[\frac{-\zeta^2}{l_{sz}^2}\right] \exp\left[-\frac{\omega\left(4i\overline{u}\xi + l_s^2\omega\right)}{4\overline{u}^2}\right]. \end{aligned} \tag{10}$$

Note that the mid-field operations result in a negative sign. It is removed because the original CPSD formulation removed a corresponding mid-field sign. Thus, the formulations are consistent. Finally, the far-field operations result in

$$\begin{aligned}
&\int_{-\infty}^{\infty} \frac{\partial^4}{\partial\tau^4}\left\{\frac{A_{ijlm}}{\pi^{1/2}\tau_s^4\omega^4}\frac{p_s p_{s,\eta} k}{c^2}\exp\left[\frac{-|\xi|}{\overline{u}\tau_s}\right]\exp\left[\frac{-(\xi-\overline{u}\tau)^2}{l_s^2}\right]\exp\left[\frac{-\eta^2}{l_{sy}^2}\right]\exp\left[\frac{-\zeta^2}{l_{sz}^2}\right]\right\}\exp\left[-i\omega\tau\right]d\tau \\
&\quad=\int_{-\infty}^{\infty}\frac{A_{ijlm}}{\pi^{1/2}\tau_s^4\omega^4}\frac{p_s p_{s,\eta} k}{c^2}\exp\left[\frac{-|\xi|}{\overline{u}\tau_s}\right]\frac{4\overline{u}^4}{l_s^8}\left(3l_s^4-12l_s^2(\xi-\overline{u}\tau)^2+4(\xi-\overline{u}\tau)^4\right)\exp\left[\frac{-(\xi-\overline{u}\tau)^2}{l_s^2}\right] \\
&\qquad\qquad\times\exp\left[\frac{-\eta^2}{l_{sy}^2}\right]\exp\left[\frac{-\zeta^2}{l_{sz}^2}\right]\exp\left[-i\omega\tau\right]d\tau \\
&\quad=\frac{A_{ijlm}}{\tau_s^4}\frac{p_s p_{s,\eta} k}{c^2}\frac{l_s}{\overline{u}}\exp\left[\frac{-|\xi|}{\overline{u}\tau_s}\right]\exp\left[\frac{-\eta^2}{l_{sy}^2}\right]\exp\left[\frac{-\zeta^2}{l_{sz}^2}\right]\exp\left[-\frac{\omega\left(4i\overline{u}\xi+l_s^2\omega\right)}{4\overline{u}^2}\right].
\end{aligned} \tag{11}$$

The results of the operations shown in Eqns. 9 through 11 are now used in conjunction with Eqn. 1, and after simplifying

$$\begin{aligned}
G\left(\boldsymbol{x}_1,\boldsymbol{x}_2,\omega\right)=\frac{1}{16\pi^2}\int_{-\infty}^{\infty}\ldots\int_{-\infty}^{\infty}\frac{A_{ijlm}p_s p_{s,\eta}k}{c^2\tau_s^4\omega^4}\frac{l_s}{\overline{u}}\left\{F_t\omega^4+M_t\omega^2+N_t\right\} \\
\times\exp\left[\frac{-\omega\left(4i\overline{u}\xi+l_s^2\omega\right)}{4\overline{u}^2}\right]\exp\left[-i\omega\left(\frac{r_1}{c_\infty}-\frac{r_2}{c_\infty}\right)\right] \\
\times\exp\left[\frac{-|\xi|}{\overline{u}\tau_s}\right]\exp\left[\frac{-\eta^2}{l_{sy}^2}\right]\exp\left[\frac{-\zeta^2}{l_{sz}^2}\right]d\boldsymbol{y}_2 d\boldsymbol{y}_1.
\end{aligned} \tag{12}$$

Equation 12 can be integrated numerically, but here we seek a simplified approach. We convert to cylindrical coordinates using the transform $\boldsymbol{y}_1 \rightarrow \boldsymbol{y}_1(y_1, z_1\cos[\phi_1], z_1\sin[\phi_1])$, where z_1 is the distance from axis y_1 to the source. Similarly we use the relation $\boldsymbol{y}_2 \rightarrow \boldsymbol{y}_2(y_2, z_2\cos[\phi_2], z_2\sin[\phi_2])$. We assume that the flow-field is axisymmetric about the centerline axis. Recall that the source of BBSAN is due to shock wave shear layer interactions. These interactions occur within very small volumes of space relative to the total volume of the jet plume. We assume that the source quantities vary very slowly spatially within the region of the shock wave shear layer interaction. These assumptions allow us to model the shock wave shear layer interactions as 'rings' of equivalent BBSAN sources centered about the nozzle axis. We note the geometric relation

$$-\frac{\left(\eta^2+\zeta^2\right)}{l_{s,r}^2}=-\frac{z_1^2+z_2^2-2z_1z_2\cos\left[\phi_1-\phi_2\right]}{l_{s,r}^2}. \tag{13}$$

Using these assumptions and Eqn. 13, Eqn. 12 is

$$\begin{aligned}
G\left(\boldsymbol{x}_1,\boldsymbol{x}_2,\omega\right)=\frac{1}{16\pi^2}\sum_{m=1}^{N_s}\sum_{n=1}^{N_s}\frac{A_{ijlm}p_s p_{s,\eta}k l_s z_1 z_2 S_x^2 S_r^2}{c^2\overline{u}\tau_s^4\omega^4} \\
\times\exp\left[\frac{-4i\overline{u}(y_2-y_1)\omega-l_s^2\omega^2}{4\overline{u}^2}\right]\exp\left[\frac{-|y_2-y_1|}{\overline{u}\tau_s}\right]\int_0^{2\pi}\int_0^{2\pi}\left\{F_t\omega^4+M_t\omega^2+N_t\right\} \\
\times\exp\left[-\frac{(z_1^2+z_2^2-2z_1z_2\cos[\phi_1-\phi_2])}{l_{s,r}^2}\right]\exp\left[-i\omega\left(\frac{r_1}{c_\infty}-\frac{r_2}{c_\infty}\right)\right]d\boldsymbol{\phi}_2 d\boldsymbol{\phi}_1,
\end{aligned} \tag{14}$$

where $l_{s,r}$ is the radial turbulent length scale, N_s is the number of shock wave shear layer interactions, and S represents the local shock thickness in the axial (x) and radial (r) directions respectively. Like the coherence and CPSD of mixing noise, the mid-field and near-field terms will have characteristic peak frequencies lower than that due to the far-field term. Turbulent mixing noise intensity is dominant in the entire flow-field at

low frequencies. Thus, we focus our attention on the far-field term when examining the BBSAN component. This does not imply that the model is invalid in the near-field or mid-field because a far-field assumption has not been made. The integration involving $\boldsymbol{\phi}_2$ and $\boldsymbol{\phi}_1$ within Eqn. 14 can now be conducted analytically. Because the shock wave shear layer interactions occur at relatively discrete locations compared to the total axial extent of the jet plume, the final axial integrals of ξ and ξ' are approximated as a double summation involving the number of shock wave shear layer interactions. The final model equation for the CPSD of BBSAN is

$$\begin{aligned} G\left(\boldsymbol{x}_1, \boldsymbol{x}_2, \omega\right) = \frac{S_x^2 S_r^2}{4 c_\infty^4} \sum_{m=1}^{N_s} \sum_{n=1}^{N_s} \frac{A_{ijlm} p_{s,m} p_{s,n} k l_s z_m z_n}{\overline{c}^2 \overline{u} \tau_s^4 r_1^2 r_2^2} \exp\left[\frac{-l_s^2 \omega^2}{4\overline{u}^2}\right] \\ \times \exp\left[\frac{-4i\overline{u}(y_2 - y_1)\omega}{4\overline{u}^2}\right] \exp\left[\frac{-|y_2 - y_1|}{\overline{u}\tau_s}\right] \exp\left[\frac{-(z_m^2 + z_n^2)}{l_{sr}^2}\right] \\ \times \exp\left[-i\omega\left(\frac{|\boldsymbol{x}_1 - \boldsymbol{y}_1|}{c_\infty} - \frac{|\boldsymbol{x}_2 - \boldsymbol{y}_2|}{c_\infty}\right)\right] I_0\left(\frac{2 r_m r_n}{l_{sr}^2}\right), \end{aligned} \tag{15}$$

where I_0 is the modified Bessel function of the first kind of order zero. Note that A_{ijlm} implies summation. Subscripts m and n imply evaluation at the m^{th} and n^{th} shock location. Equation 15 is in closed-form with special function I_0 and can be used to predict the cross-spectrum from the shock wave shear layer interactions of axisymmetric jet flows.

We must model the arguments of Eqn. 15 that are associated with the turbulence within the jet. The remaining terms need to be modeled. They could be found through numerical computation, but here we rely on empirical models generated from measurements. The core length of the jet, y_c, is approximated using the equation of Eggers[32] and modified by Tam et al.[17]

$$\frac{y_c}{D_j} = \begin{cases} 4.2 + 1.1 M_j^2 + 1.1(1 - T_j/T_\infty) & \text{for } T_j < T_\infty \\ 4.2 + 1.1 M_j^2 + \exp[-3.2(T_j/T_\infty - 1)] - 1 & \text{for } T_j \geq T_\infty, \end{cases} \tag{16}$$

where T_j is the fully-expanded temperature. The number of shocks within the jet plume, N_s, is estimated by performing the maximization

$$N_s := \arg\max_{N_s} \left\lfloor y_c \geq D_j \left\{ \left(1 + \frac{\sqrt{2}}{20}\right) N_s \beta + \frac{\sqrt{2} - 1}{10} N_s + \frac{233}{2500} \right\} \right\rfloor. \tag{17}$$

Equation 17 is based partly upon the theory of Pack[19] and calibrated by examining the number of shock wave shear layer interactions within a database of off-design jet steady RANS solutions. The fully-expanded diameter, D_j, is adopted from Tam and Tanna.[7] Equation 15 assumes sources are at relatively discrete locations. These locations are estimated using the theory of Pack,[19] and a simplifying assumption that they reside on the sonic line that extends roughly from the nozzle lip, $\boldsymbol{y}_i = \boldsymbol{y}_i(0, D_j/2, \phi)$, to approximately the end of the potential core, $\boldsymbol{y}_i \approx \boldsymbol{y}(y_c, 0, 0)$. The shock pressure, $p_{s,i}$, at each shock wave shear layer interaction, $i = 2$ to N_s is based upon a linear estimation

$$p_{s,i} = -\Delta p \, \frac{y_{i-1}}{y_{N_s}} + \Delta p + p_\infty, \tag{18}$$

where $p_{s,i} = \Delta p + p_\infty$ for $i = 1$ and the isentropic formula

$$\Delta p = p_t \left(1 + \frac{\gamma - 1}{2} M_d^2\right)^{-\frac{\gamma}{\gamma - 1}} - p_\infty. \tag{19}$$

Here p_t is the total pressure in the nozzle plenum. The streamwise velocity component is estimated using the empirical formula of Witze[33]

$$\overline{u} = \begin{cases} u_j & \text{for } y_1 < y_c \\ u_j \left(1 - \exp\left[1.35(1 - y_i/y_c)^{-1}\right]\right) & \text{for } y_1 \geq y_c, \end{cases} \tag{20}$$

and convection velocities are estimated by multiplying $\overline{u}$ by 0.70. The variation of temperature, $\overline{T}$, is assumed to possess the same form as the empirical relation for $\overline{u}$. The variation of the speed of sound is $\overline{c} = \left(\gamma R\overline{T}\right)^{1/2}$ and the variation of density is $\overline{\rho} = (p_\infty + p_{s,i})(R\overline{T})^{-1}$. Scales of turbulence are estimated by

$$l_s = l_c \left(\frac{1}{2} D_j + \alpha_1 y_1 D_j\right) \exp\left[-\frac{1}{10} \ln\left[\frac{\tilde{\omega}^2}{\omega_1 \omega_2}\right]\right], \tag{21}$$

where $\alpha_1 = 0.138 D^{-1}$ and l_c is a constant, $\tilde{\omega} = \omega(1 - \cos[\theta_1]/2)(1 - \cos[\theta_2]/2)$ is the modified frequency, and $\omega_i = 2\pi u_c u_j \left(1 - u_c M_j \cos\theta_i\right)^{-1} (y_2 - y_1)^{-1}$ is the peak frequency. Here θ_i is the observer angle from local shock wave shear layer interactions to observer i. The first term of Eqn. 21 involving D_j enforces the growth of the length scale as the flow develops from the nozzle exit, and the second term contains frequency dependence. Frequency dependence of the length scale is inspired by the work of Lieb and Goldstein[34] and Morris and Boluriaan.[35] Separation between shocks within the second term is also included to emphasize the importance that large spatially coherent turbulence is responsible for BBSAN generation. The radial turbulent length scale is one-third the axial length scale. The time scale of turbulence, τ_s, is modeled as

$$\tau_s = \frac{\tau_c l_s}{u_c \overline{u}} \tanh\left[\frac{4\omega}{(\omega_1 + \omega_2)}\right]^{-2}, \tag{22}$$

where τ_c is a constant. Here, τ_s also contains frequency dependence and shock separation distance within its second factor and is consistent with Eqn. 21. The variation of turbulent kinetic energy, k, is modeled as a log-normal distribution

$$k = \alpha_3 u_j^2 \exp\left[-\alpha_2^{-1} \ln\left[\frac{y_1}{y_c}\right]^2\right] \tag{23}$$

and is calibrated empirically relative to the measurements of Bridges and Wernet,[10] where $\alpha_2 = 1$ and $\alpha_3 = 11/300$ are constants. Unfortunately, Eqn. 23 does not account for the large increases of k near each shock wave observed in measurements of off-design jets.

Now that the arguments of the model involving an equivalent meanflow and basic turbulence statistics have been proposed, we can form a model for the coefficient matrix A_{ijlm}

$$\begin{aligned} A_{ijlm} = P_f^2 \exp\left[-(\phi_1 - \phi_2)^2 \left\{1 + \tilde{St}^4 \left(\frac{3}{100} \frac{u_c (1 - u_c M_j \cos\theta_1)^{-1}}{D_j \Delta}\right)^{-1}\right\}\right] \\ \times \exp\left[\frac{10}{3}(\theta_1 - \theta_2)^2 St^{1/2} \left(\frac{1}{2} + \frac{1}{2}\tanh[3(\theta_2 - \pi/3)]\right)\right] \\ \times \exp\left[\frac{-[l_s^2(\omega^2 - \tilde{\omega}^2) + 4i\overline{u}(y_2 - y_1)(\omega - \tilde{\omega})]}{4\overline{u}^2}\right], \end{aligned} \tag{24}$$

where P_f is a constant, St is the Strouhal number based on u_j and D_j, a tilde denotes that the modified frequency is used, and Δ is the axial distance between the first and second shock wave. Equation 24 is in a similar form to that proposed by Miller[26] for mixing noise cross-spectra, and its justification is discussed there. It contains two (relatively weak) terms that are dependent on the radiation directions and frequency.

The prediction of spatial coherence is performed by evaluating

$$\Gamma(\boldsymbol{x}_1, \boldsymbol{x}_2, \omega) = \frac{G(\boldsymbol{x}_1, \boldsymbol{x}_2, \omega) G^*(\boldsymbol{x}_1, \boldsymbol{x}_2, \omega)}{G(\boldsymbol{x}_1, \boldsymbol{x}_1, \omega) G(\boldsymbol{x}_2, \boldsymbol{x}_2, \omega)}, \tag{25}$$

where the superscript $*$ represents the complex conjugate. The evaluation of Γ requires three separate evaluations of Eqn. 15. Equation 15 can now be evaluated using these simple models based on experimentally or numerically observed trends.

Results

This section shows comparisons of predicted auto-spectra and coherence of BBSAN using Eqn. 15 with various measurements. Comparisons of auto-spectra and spatial coherence are shown in the near-field and far-field. Measurements are obtained from various facilities, and their diversity demonstrates the robustness of the method.

Far-Field Auto-Spectra

Predictions using Eqn. 15 for power spectral density (PSD) in the far-field are compared with measurement. Comparisons are shown on a non-dimensional basis using St and adjusting SPL to unit St via addition of $10\log_{10}\left[u_j D_j^{-1}\right]$ to the PSD. Measurements are obtained from Bridges and Brown[9] that were conducted at the Small Hot Jet Acoustic Rig (SHJAR) facility of NASA. We examine measurements from two axisymmetric nozzles from the SHJAR database. The first nozzle is conical and convergent with M_d of unity, and the second nozzle is designed with the method of characteristics with $M_d = 1.50$. Both nozzles have an exit diameter of $D = 0.0508$ m. Both over- and under-expanded, and heated and cold, conditions are shown. Microphones are located on a circular arc centered about the nozzle exit and measurements are corrected to a distance of $R = 100D$ by accounting for spherical spreading. Comparisons are conducted on a lossless basis, and measurements account for associated atmospheric absorption effects.

Eight far-field conditions are considered. The first is shown in Fig. 1 for the convergent nozzle operating at $M_j = 1.24$ and TTR = 1.00. Solid lines represent the measurement from the SHJAR facility of Bridges and Brown,[9] and the dashed lines represent the predictions from Eqn. 15. The x-axis is St and the y-axis is SPL per unit St. There are five sets of comparisons at observer angles $\Psi = 50$ through 130 degs. separated by 20 deg. increments. Note that the y-axis lines are 30 ΔdB apart and the maximum broadband SPL per unit St level is written next to each measurement. The observer angle is measured from the upstream nozzle axis. Recall that the measurement represents the total noise and the prediction is only for the BBSAN component of the total noise spectrum. Predictions are in agreement with measurement with respect to the maximum BBSAN intensity and peak frequency. Multiple broad lobes are apparent in the upstream and sideline observer directions, and in the downstream direction broaden significantly. At frequencies lower than $St \approx 0.3$ the predictions fall-off quickly as the frequency bands are dominated by noise from turbulent mixing. At higher frequencies the predictions fall-off from measurement, and the reason for this is discussed below.

We now examine the same moderately off-design condition from the convergent nozzle operating at $M_j = 1.24$ and increase the heating to TTR = 3.20. Predictions are compared with measurement in Fig. 2. Relative to Fig. 1, it is apparent that the addition of heating has eliminated the many shock-associated tones. In actuality the BBSAN intensity is relatively insensitive to changes in temperature as shown recently by Viswanathan et al.,[3] Kuo et al.,[12] and Miller.[4] Predictions show the same level of agreement as the unheated case, where the peak intensity and peak frequency match measurement.

Two highly off-design comparisons are shown in Figs. 3 and 4. The convergent nozzle operates at $M_j = 1.47$, and TTR = 1.00 or TTR = 3.20. Screech tones are present within both measurements. The unheated case in Fig. 3 shows relatively less agreement than the heated case. This is partly due to the effect of heating on the acoustic feedback loop within the jet plume. In all directions the peak predicted intensities are lower than measurement. This is not the case for the heated comparison at $M_j = 1.47$.

A final heated comparison for the convergent nozzle is shown in Fig. 5. The jet operates at $M_j = 1.57$ and TTR = 3.20. The spectrum at the sideline location is used to calibrate the coefficients present within Eqn. 15. Once the coefficients are calibrated, they are held constant irrespective of the jet operating conditions. It comes as no surprise that the spectral shape of the main BBSAN lobe matches the measurement. No optimization algorithm is used for this task, and certainly more optimized values can be chosen. In the upstream direction the peak intensity and peak frequency continue to agree with measurement. Unfortunately, in the downstream radiation direction the spectral width of the BBSAN does not increase, as observed for select cases. It is emphasized that an optimized set of coefficients would increase the agreement for all predictions, but that is not the purpose of this investigation.

We now turn our attention to the convergent-divergent method of characteristics nozzle with $M_d = 1.50$. Figure 6 shows comparisons of predictions using Eqn. 15 with measurements from the nozzle operating at $M_j = 1.294$ and TTR = 1.00. This flow is over-expanded unlike the others considered. The over-pressure of the tonal components is larger than other cases examined, and this highly affects the BBSAN component. The predicted low and high frequency BBSAN fall-off is too small and large, respectively.

Two final far-field auto-spectral comparisons are shown in Figs. 7 and 8. The $M_d = 1.50$ nozzle operates under-expanded at $M_j = 1.70$ and $M_j = 1.828$. Both flows are unheated. In general the overall trends are captured. It is interesting that for the $M_j = 1.70$ case the higher frequency components are captured by the model. Otherwise, the same trends are observed in these comparisons as those previously examined.

The auto-spectral predictions shown here often exhibit a higher rate of intensity fall-off relative to measurement. Particular predictions of Morris and Miller[23] also showed this behavior to a lesser extent. The

method of Tam[20,22] used an empirical correction factor to control the intensity decay with frequency at high frequencies. Harper-Bourne and Fisher[1] avoided this problem by using a master source spectrum that was calibrated with measurement. An empirical correction, such as the one developed by Tam,[20,22] can easily be used to correct the high frequency intensity decay.

The predicted peak intensities at the BBSAN peak frequency compared very favorably across the jet operating conditions examined at the sideline location. Refraction effects within the jet shear layer have little effect on the intensity of waves propagating to the far-field in the sideline direction. These observations give credibility to the equivalent source model of Eqn. 7. This choice of equivalent source combined with other model arguments allows for the majority of the characteristics of BBSAN to be predicted satisfactorily.

Near-Field Auto-Spectra

We now turn our attention to examining the characteristics of the BBSAN intensity in the jet near-field. For this task we use the excellent measurements of Yu.[5] Yu[5] conducted near-field measurements using a convergent-divergent nozzle with exit diameter of $D = 0.0508$ m. The jet operates at $M_j = 1.67$ and TTR $= 1.00$. Coincidently, this operating condition is almost identical to that presented for far-field auto-spectral comparisons as shown in Fig. 7. Yu[5] used a near-field microphone array that transversed in the axial and radial directions over a very large spatial range. Measurements were processed by Yu in one-third octave center bands and presented as contour plots. Spatial dimensions are normalized by the nozzle exit diameter and an off-set in the radial direction of one-half D. It must be emphasized that the prediction model is for BBSAN and not shock-associated tones or turbulent mixing noise. It is expected that there will be some differences between prediction and measurement for this reason.

Figure 9 shows near-field contours of SPL in the 16 kHz one-third octave center band from the $M_j = 1.67$ off-design unheated jet. Contours are labeled by the local sound pressure level. The predicted levels are shown in Fig. 9(a) and the measured levels are shown in Fig. 9(b). The broad black line within the measurement was used by Yu to illustrate the region where microphones were not present. At this relatively low frequency (for a laboratory scale nozzle) a single broad lobe appears within both the predicted and measured contours that is directed slightly upstream relative to the sideline direction. Very close to the shock wave shear layer interactions ($0 < x/D < 10$ and $0 < r < D/2$) the predictions show wavefronts surrounding the sources. Predictions have high enough resolution to capture the very near-field behavior while measurements lack detail. The agreement of overall levels and directivity at this frequency is fairly good, and as an example the contour level of 132 dB occurs both in prediction and measurement near $x/D \approx 2.5$ and $r/D - 1/2 \approx 15$.

The same jet near-field is now examined at the 25 kHz one-third octave center band. These comparisons are shown in Fig. 10. Here, a single broad lobe is again present and its directivity remains close to the sideline direction. Relative to the previous comparison, the prediction is overall slightly less intense and points slightly more downstream. The measured contours of Yu[5] have a considerably thiner width, and the predicted contours are upstream by a few diameters.

Figure 11 shows SPL contours at 31.5 kHz one-third octave center band. At this higher frequency we start to observe the formation of a second contour lobe in the upstream direction that is not present at lower frequencies. The more intense lobe has a directivity at a larger observer angle. Compared to the measurement the predicted intensity is slightly farther upstream and radiates at a slightly lower intensity.

A final comparison of contours of SPL and measurements of Yu[5] is shown in Fig. 12. At the 40 kHz one-third octave band frequency the dominant radiation direction of both lobes is shifted to larger observer angles. The measurement also shows stronger double lobes. Contour levels between the two maps differ by a couple one-third octave dB and show some spatial shift.

As an exercise we examine the region very close to the shock wave shear layer interactions of the off-design jet of Yu.[5] The $M_d = 1.50$ nozzle operates at $M_j = 1.67$ and TTR $= 1.00$. Figure 13 shows contours of BBSAN intensity at one-third octave bands of 16, 25, 31.5, and 40 kHz. The contour maps are consistent between figures. Regions of high intensity near the nozzle lip line are very close to the shockwave shear layer interactions. By examining the contours near each shock wave shear layer interaction, it is clear that the complexity of the flow-field increases with increasing frequency. Finally, an important point of this theory is the highest intensity sources are located at multiple shocks downstream from the nozzle exit, and this is corroborated by other measurements that used beam-forming. This is mainly due to the growth of the intensity of turbulent kinetic energy with increasing axial distance from the nozzle exit and the turbulent kinetic energy interactions with the shock waves.

Far-Field Coherence

Predicted spatial coherence in the jet far-field is now compared with measurements of Viswanathan et al.[3] We focus on the comparison of coherence due to its relevance to practical problems. Predicted coherence is governed by Eqn. 25. The arguments of Eqn. 25 are provided by the developed model Eqn. 15. Note that to evaluate coherence between two observer positions ($\boldsymbol{x}_1$ and $\boldsymbol{x}_2$) the cross-spectral prediction using Eqn. 25 is evaluated three times. Coherence is examined by holding the observer $\boldsymbol{x}_1$ constant while varying the azimuthal position of observer $\boldsymbol{x}_2$. Reversing the two observer positions results in the same coherence.

Figure 14 shows predicted coherence compared with measurements of Viswanathan et al.[3] These measurements were conducted by Viswanathan et al.[3] using a convergent nozzle with exit diameter of $D = 0.06223$ m. Multiple microphones were located on an azimuthal arc in ten degree increments at the sideline direction. The nozzle operated at $M_j = 1.57$ and TTR = 3.20. The solid lines within Fig. 14 represent the coherence calculated by Viswanathan et al.[3] and the dashed lines are predictions using Eqn. 25. Four variations of azimuthal angle separation are shown at $\Delta\phi = 10$, 20, 30, and 40 degs. As the azimuthal angle increases the coherence diminishes from a maximum of approximately 0.90 to 0.46. For this particular jet flow the high levels of coherence from turbulent mixing are present in the range of $0.001 \lessapprox St \lessapprox 0.1$. Coherence due to the BBSAN source is approximately in the range of $0.1 \lessapprox St \lessapprox 1.0$. Coherence at higher frequencies is almost negligible for this particular jet operating condition in the far-field; however, for other jet operating conditions significant coherence might be present due to mixing noise or possibly shock-associated noise. The predicted maximum amplitude of coherence and peak frequency of coherence are in close agreement with measurements. The predicted envelope of coherence is perhaps too wide relative to measurement.

The same nozzle and microphone array of Viswanathan et al.[3] are used to make a second comparison shown in Fig. 15. The convergent nozzle operates at $M_j = 1.24$ and TTR = 3.20. At this more conservative off-design condition the azimuthal coherence variation follows the same general trend as shown in Fig. 14. The spatially varying coherence due to the off-design condition is apparent as a broad lobe near the BBSAN peak frequency and intensity. Predicted peak coherence is within approximately 0.1 of measurement for the four angles examined.

Near-Field Coherence

Final comparisons are shown for spatial coherence in the jet near-field using Eqns. 15 and 25. Because the model is developed for the near-field, no alteration of the equations or their evaluation is required. Figure 16 shows comparisons of predicted coherence with the measurements of Savarese et al.[13] Measurements were conducted with a convergent contoured nozzle with exit diameter of 0.04 m operating at $M_j = 1.22$ and TTR = 1.00. A linear microphone array was located at $R/D = 4$ radially from the nozzle centerline axis and was parallel to the nozzle centerline axis. Each microphone was separated by a distance of $0.625D$. The reference microphone ($\boldsymbol{x}_1$) is located at the sideline location and $R/D = 4$. Observer positions of $\boldsymbol{x}_2$ are located at $\Delta x/D$ = -1.250, -0.625, 0.625, and 1.250. Predictions and measurements follow the same trends and show the same agreement as the far-field comparisons. In the near-field, there is much more variation in coherence, especially at higher frequencies, and a strong screech tone is present near $St \approx 0.45$. At frequencies higher than $St \approx 1$, there is a combination of coherent nozzle tones (as discussed by Suzuki and Colonius[36]) and some coherence due to BBSAN. The maximum predicted coherence matches the measured maximum near the BBSAN peak coherent frequency fairly well except for $\Delta x/D = 0.625$, where it is lower by approximately 0.1. The peak frequencies are well predicted; that is to be expected relative to the far-field results.

Two additional comparisons are shown using the predictions of Eqn. 15 and the measurements of Savarese et al.[13] These are presented in Figs. 17 and 18. Fully-expanded Mach numbers are 1.16 and 1.28 respectively, and the other jet conditions and observer locations remain the same. Like the previous near-field case, as the axial distance increases the coherence magnitude decreases. The width of the BBSAN coherence generally captures the main BBSAN lobe. Higher and lower frequency coherence is likely due to other sources due to their dominance of the BBSAN within the pressure time history.

Comparisons of predictions of acoustic intensity or coherence in the near-field are difficult given the large number of aerodynamic effects. The measurements are equally difficult. Because of the agreement of intensity in the far-field and near-field and coherence in the far-field, some confidence is obtained for the prediction of coherence due to shock wave shear layer interactions in the near-field. The relative maximum BBSAN coherence and peak frequency in the near-field seems to be correctly predicted, though there is additional coherence at $St > 1$ that is likely due to aerodynamic effects or other noise sources.

Conclusion

The cross-spectral acoustic analogy is used to predict auto-spectra and coherence of broadband shock-associated noise (based on cross-spectra) within the jet near-field and far-field. An equivalent source term is proposed for the shock-associated noise source that is consistent with other models for BBSAN. Arguments of the model involve flow-field statistics near the shock wave shear layer interactions. These arguments are dependent on the jet Mach number, temperature ratio, and nozzle exit diameter. A simplified model is developed based on the assumption that the flow is axisymmetric, and its arguments are dependent on a variety of measurements. The resultant model consists of a double summation of the source over all shock wave shear layer interactions.

It is shown that predictions of auto-spectra and coherence generally compare favorably for a wide range of jet Mach numbers and temperature ratios. This observation gives credibility to the choice of the equivalent source model, which is satisfying given that refraction effects are not explicitly accounted for within this approach. Auto-spectral predictions exhibit a high rate of intensity fall-off relative to measurement, and this can easily be altered with an empirical correction factor. Near-field auto-spectral predictions correctly capture the formation of increasing numbers of directional lobes that originate from the shock cell structure. There are large variations of intensity between each shock wave shear layer interaction as observed in the amplified view of the contours. Though, there is some axial shift within the predictions relative to measurement, their intensities are relatively similar. The complexity of coalescence of radiating broadband shock-associated noise increases greatly with increasing frequency. High intensity sources are located at multiple shock wave shear layer interactions downstream from the nozzle exit, and this is corroborated with measurements using beam-forming. The log-normal model for turbulent kinetic energy is essential for capturing this trend.

At mid-frequencies within the near-field or far-field, strong broad lobes of coherence are due to shock wave shear layer interactions, while at lower and higher frequencies this coherence is due to other effects. Measured coherence in the near-field contains additional near-field effects due to other sources and additional hydrodynamic fluctuations. Unfortunately, in some cases the predicted envelope of the coherence is too wide relative to measurement. Predicted near-field coherence is nearly zero at high frequencies, and measurement shows coherent tones dominating high frequencies. It is likely that the spatial BBSAN coherence is nearly zero at high frequencies based upon the far-field comparisons, where strongly coherent nozzle tones are not present. Given the wide range of nozzle operating conditions and the difficulty of the measurements, predictions capture the overall trends of the statistics of the near-field shock-associated noise satisfactorily.

Acknowledgments

The author is grateful for continuous support from the National Aeronautics and Space Administration (NASA), Advanced Air Vehicles Program, Commercial Supersonic Technology Project. This research is possible due to the availability of measurement data from Alessandro Savarese of The Airbus Group, James Bridges of NASA Glenn Research Center, and Krishnamurthy Viswanathan of The Boeing Company. Alessandro Savarese is most gracious by providing tailored near-field measurements to the author.

References

[1]Harper-Bourne, M. and Fisher, M. J., "The Noise from Shock-Waves in Supersonic Jets," AGARD Conference Proceedings, 1973.

[2]Norum, T. D. and Seiner, J. M., "Broadband Shock Noise from Supersonic Jets," *AIAA Journal*, Vol. 20, No. 1, 1982, pp. 68–73. doi:10.2514/3.51048.

[3]Viswanathan, K., Alkislar, M. B., and Czech, M. J., "Characteristics of the Shock Noise Component of Jet Noise," *AIAA Journal*, Vol. 48, No. 1, 2010, pp. 25–46. doi:10.2514/1.38521.

[4]Miller, S. A. E., "The Scaling of Broadband Shock-Associated Noise with Increasing Temperature," *International Journal of Aeroacoustics*, Vol. 14, No. 1-2, 2015.

[5]Yu, J. C., "Investigation of the Noise Fields of Supersonic Axisymmetric Jet Flows," *Ph.D. Thesis, Syracuse University*, 1971.

[6]Tanna, H. K., "An Experimental Study of Jet Noise Part II: Shock Associated Noise," *Journal of Sound and Vibration*, Vol. 50, No. 3, 1977, pp. 429–444. doi:10.1016/0022-460X(77)90494-1.

[7]Tam, C. K. W. and Tanna, H. K., "Shock-Associated Noise of Supersonic Jets from Convergent-Divergent Nozzles," *Journal of Sound and Vibration*, Vol. 81, No. 3, 1982, pp. 337–358. doi:10.1016/0022-460X(82)90244-9.

[8]Seiner, J. M. and Yu, J. C., "Acoustic Near-Field Properties Associated with Broadband Shock Noise," *AIAA Journal*, Vol. 22, No. 9, 1984, pp. 1207–1215. doi:10.2514/3.8762.

[9]Bridges, J. and Brown, C. A., "Validation of the Small Hot Jet Acoustic Rig for Aeroacoustic Research," *11th AIAA/CEAS Aeroacoustics Conference, Monterey, California, 23 - 25 May, AIAA Paper 2005-2846*, 2005. doi:10.2514/6.2005-2846.

[10]Bridges, J. and Wernet, M. P., "Turbulence Associated with Broadband Shock Noise in Hot Jets," *14th AIAA/CEAS Aeroacoustics Conference, Vancouver, British Columbia, 5 - 7 May, AIAA Paper 2008-2834*, 2008. doi:10.2514/6.2008-2834.

[11]Panda, J., "Measurement of Shock Oscillation in Underexpanded Supersonic Jets," *26th AIAA Fluid Dynamics Conference, AIAA Paper 95-2145*, 1995. doi:10.2514/6.1995-2145.

[12]Kuo, C., McLaughlin, D. K., and Morris, P. J., "Effects of Supersonic Jet Conditions on Broadband Shock-Associated Noise," *49th AIAA Aerospace Sciences Meeting, AIAA Paper 2011-1032*, 2011. doi:10.2514/6.2011-1032.

[13]Savarese, A., Jordan, P., Royer, A., Fourment, C., Collin, E., Gervais, Y., and Porta, M., "Experimental Study of Shock-Cell Noise in Underexpanded Supersonic Jets," *19th AIAA/CEAS Aeroacoustics Conference, AIAA Paper 2013-2080*, 2013. doi:10.2514/6.2013-2080.

[14]Norum, T. D. and Shearin, J. G., "Shock Noise from Supersonic Jets in Simulated Flight to Mach 0.4," *10th AIAA/CEAS Aeroacoustics Conference, AIAA Paper 86-1945*, 1986. doi:10.2514/6.1986-1945.

[15]Ahuja, K. K., Tanna, H. K., and Tester, B. J., "Effects of Simulated Forward Flight on Jet Noise, Shock Noise, and Internal Noise," *5th AIAA Aeroacoustics Conference, Seattle, Washington, 12 - 14 March, AIAA Paper 79-0615*, 1979. doi:10.2514/6.1979-615.

[16]Harper-Bourne, M., "On Modelling the Near-Field Noise of the High-Speed Jet Exhausts of Combat Aircraft," *8th AIAA/CEAS Aeroacoustics Conference, AIAA Paper 2002-2424*, 2002. doi:10.2514/6.2002-2424.

[17]Tam, C. K. W., Jackson, J. A., and Seiner, J. M., "A Multiple-Scales Model of the Shock-Cell Structure of Imperfectly Expanded Supersonic Jets," *Journal of Fluid Mechanics*, Vol. 153, 1985, pp. 123–149. doi:10.1017/S0022112085001173.

[18]Tam, C. K. W. and Jackson, J. A., "On the Shock Cell Structure and Noise of Supersonic Jets," *8th AIAA Aeroacoustics Conference, AIAA Paper 83-0703*, 1983. doi:10.2514/6.1983-703.

[19]Pack, D. C., "On the Formation of Shock-Waves in Supersonic Gas Jets: Two-Dimensional Flow," *Quarterly Journal of Mechanics and Applied Mathematics*, Vol. 1, No. 1, 1948, pp. 1–17. doi:10.1093/qjmam/1.1.1.

[20]Tam, C. K. W., "Stochastic Model Theory of Broadband Shock-Associated Noise from Supersonic Jets," *Journal of Sound and Vibration*, Vol. 116, No. 2, 1987, pp. 265–302. doi:10.1016/S0022-460X(87)81303-2.

[21]Tam, C. K. W. and Chen, K. C., "A Statistical Model of Turbulence in Two-Dimensional Mixing Layers," *Journal of Fluid Mechanics*, Vol. 92, No. 2, 1979, pp. 303–326. doi:10.1017/S002211207900063X.

[22]Tam, C. K. W., "Broadband Shock-Associated Noise of Moderately Imperfectly-Expanded Supersonic Jets," *Journal of Sound and Vibration*, Vol. 140, No. 1, 1990, pp. 55–71. doi:10.1016/0022-460X(90)90906-G.

[23]Morris, P. J. and Miller, S. A. E., "Prediction of Broadband Shock-Associated Noise Using Reynolds-Averaged Navier-Stokes Computational Fluid Dynamics," *AIAA Journal*, Vol. 48, No. 12, 2010, pp. 2931–2944. doi:10.2514/1.J050560.

[24]Miller, S. A. E. and Morris, P. J., "The Prediction of Broadband Shock-Associated Noise Including Propagation Effects," *International Journal of Aeroacoustics*, Vol. 11, No. 8, 2012, pp. 755–782. doi:10.1260/1475-472X.11.7-8.755.

[25]Miller, S. A. E., "Toward a Comprehensive Model of Jet Noise using an Acoustic Analogy," *AIAA Journal*, Vol. 52, No. 10, 2014, pp. 2143–2164. doi:10.2514/1.J052809.

[26]Miller, S. A. E., "Prediction of Near-Field Jet Cross Spectra," *AIAA Journal*, 2015. doi:10.2514/1.J053614.

[27]Lighthill, M. J., "On Sound Generated Aerodynamically. I. General Theory," *Proc. R. Soc. Lond. A.*, Vol. 211, No. 1107, 1952, pp. 564–587. doi:10.1098/rspa.1952.0060.

[28]Lighthill, M. J., "On Sound Generated Aerodynamically. II. Turbulence as a Source of Sound," *Proc. R. Soc. Lond. A.*, Vol. 222, No. 1148, 1954, pp. 1–32. doi:10.1098/rspa.1954.0049.

[29]Lighthill, M. J., "Aerodynamic Noise, or, Turbulence as a Source of Sound," *Fluid Motion Sub-Committee Aeronautical Research Council*, 1950, pp. 1–26.

[30]Ribner, H., "Theory of Two-Point Correlations of Jet Noise," *NASA TN D-8330*, 1976.

[31]Ffowcs Williams, J. E., "The Noise from Turbulence Convected at High Speed," *Phil. Trans. R. Soc. Lond. A*, Vol. 255, No. 1063, 1963, pp. 469–503. doi:10.1098/rsta.1963.0010.

[32]Eggers, J. M., "Velocity Profile and Eddy Viscosity Distributions Downstream of a Mach 2.2 Nozzle Exhausting to Quiescent Air," *NASA TN D-3601*, 1966.

[33]Witze, P. O., "Centerline Velocity Decay of Compressible Free Jets," *AIAA Journal*, Vol. 12, No. 4, 1974, pp. 417–418. doi:10.2514/3.49262.

[34]Leib, S. and Goldstein, M. E., "Hybrid Source Model for Predicting High-Speed Jet Noise," *AIAA Journal*, Vol. 49, No. 7, 2011, pp. 1324–1335. doi:10.2514/1.J050707.

[35]Morris, P. J. and Boluriaan, S., "The Prediction of Jet Noise From CFD Data," *10th AIAA/CEAS Aeroacoustics Conference, AIAA Paper 2004-2977*, 2004.

[36]Suzuki, T. and Colonius, T., "Identification of Jet Instability Waves and Design of a Microphone Array," *10th AIAA/CEAS Aeroacoustics Conference, AIAA Paper 2004-2960*, 2004. doi:10.2514/6.2004-2960.

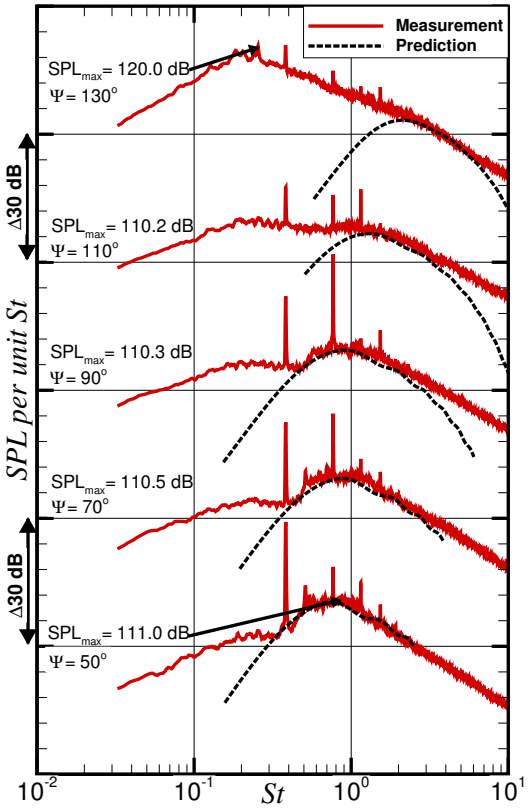

Figure 1. Predictions of BBSAN intensity compared with measurement for $M_d = 1.00$, $M_j = 1.24$, and TTR = 1.00.

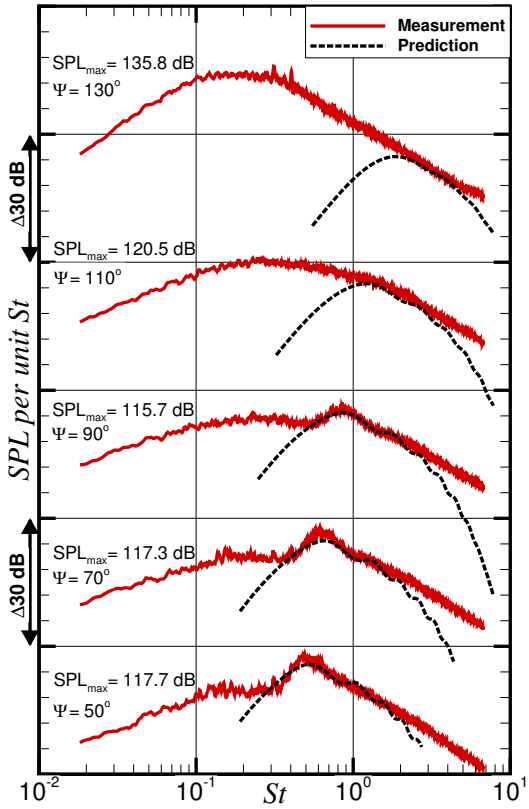

Figure 2. Predictions of BBSAN intensity compared with measurement for $M_d = 1.00$, $M_j = 1.24$, and TTR = 3.20.

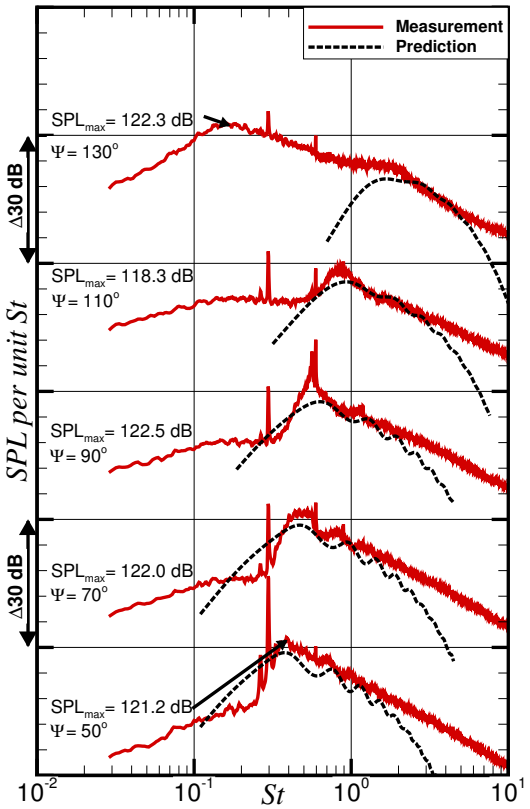

Figure 3. Predictions of BBSAN intensity compared with measurement for $M_d = 1.00$, $M_j = 1.47$, and TTR = 1.00.

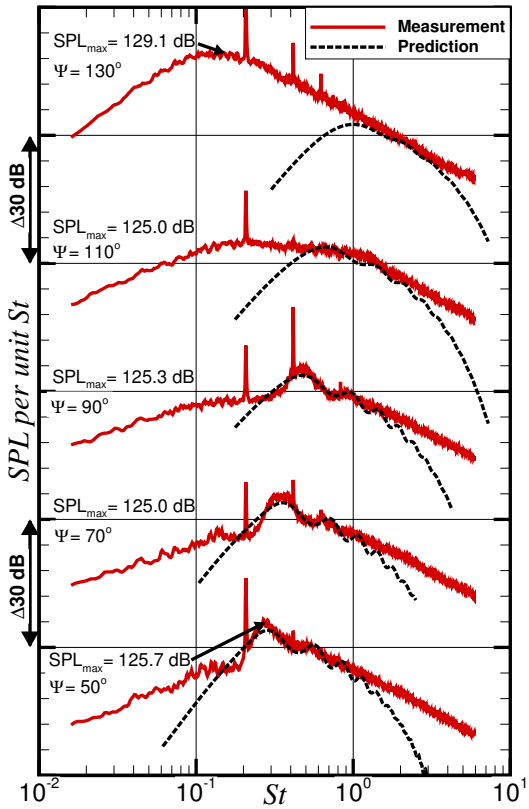

Figure 4. Predictions of BBSAN intensity compared with measurement for $M_d = 1.00$, $M_j = 1.47$, and TTR = 3.20.

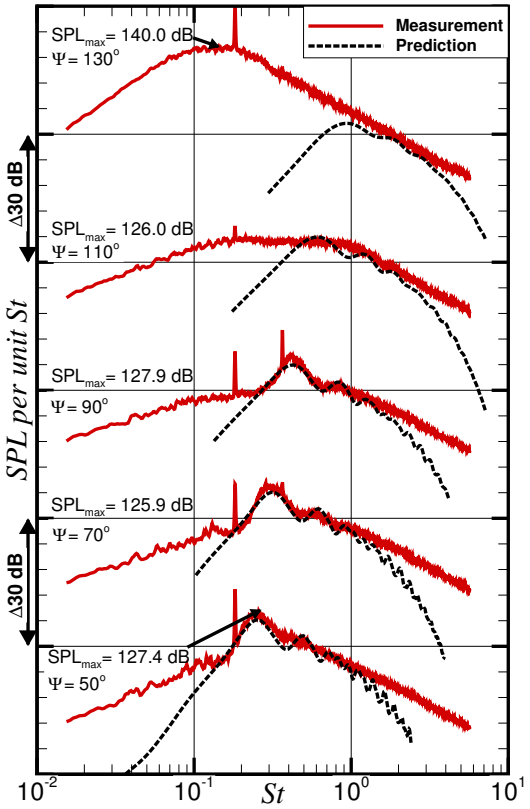

Figure 5. Predictions of BBSAN intensity compared with measurement for $M_d = 1.00$, $M_j = 1.57$, and TTR = 3.20.

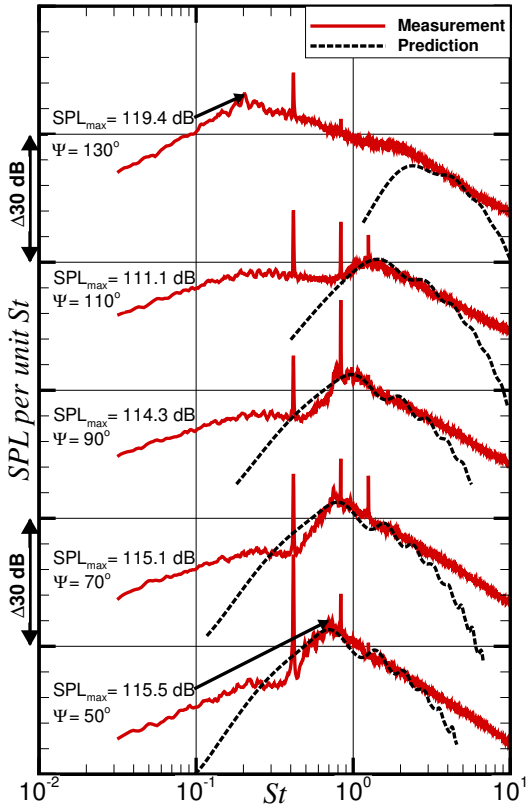

Figure 6. Predictions of BBSAN intensity compared with measurement for $M_d = 1.50$, $M_j = 1.294$, and TTR = 1.00.

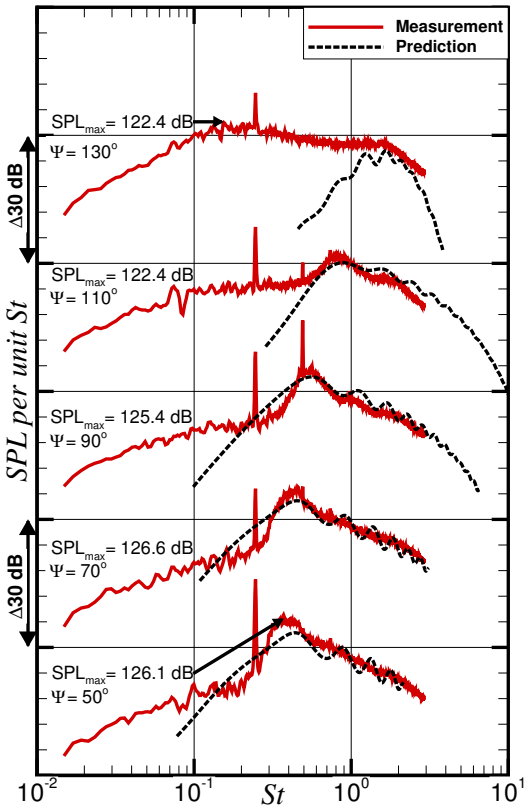

Figure 7. Predictions of BBSAN intensity compared with measurement for $M_d = 1.50$, $M_j = 1.70$, and TTR = 1.00.

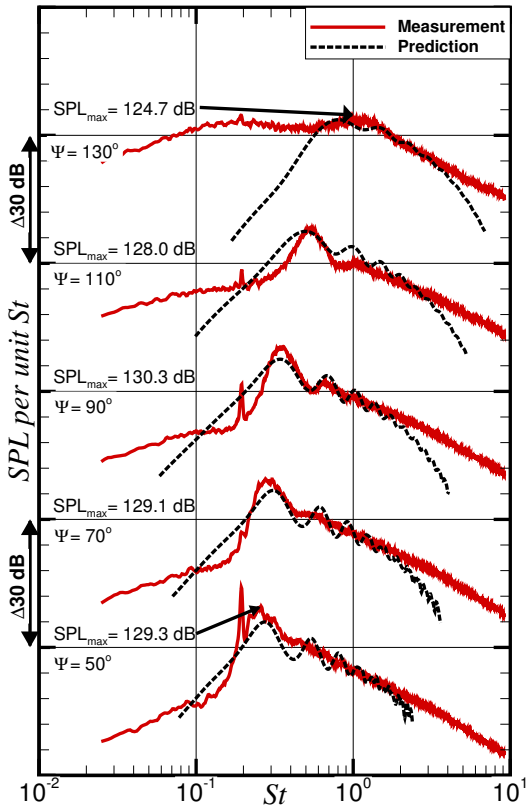

Figure 8. Predictions of BBSAN intensity compared with measurement for $M_d = 1.50$, $M_j = 1.828$, and TTR = 1.00.

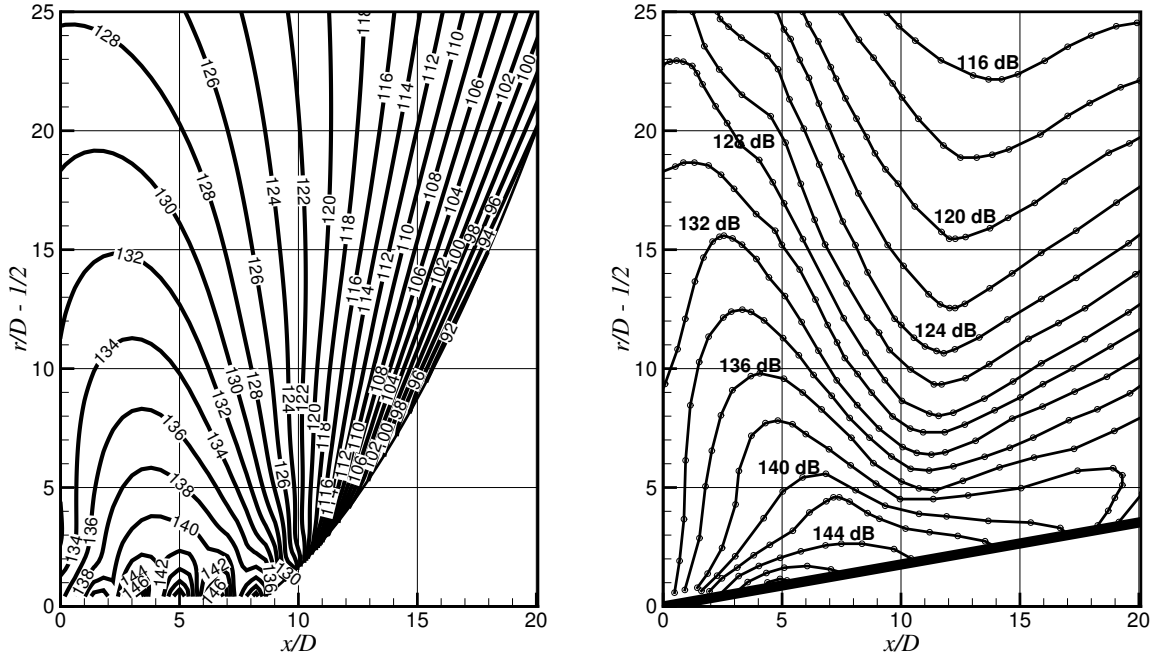

(a) BBSAN Prediction (b) Measurement

Figure 9. Near-field contours of SPL at 16 kHz. The $M_d = 1.50$ nozzle operates at $M_j = 1.67$ and TTR = 1.00.

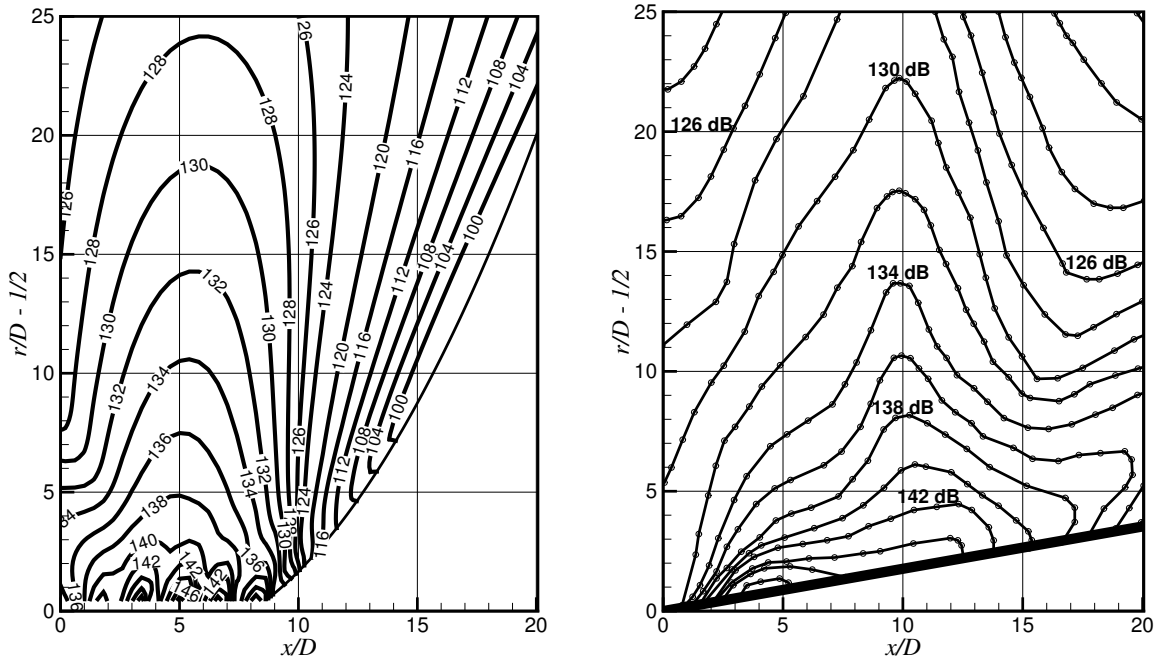

(a) BBSAN Prediction (b) Measurement

Figure 10. Near-field contours of SPL at 25 kHz. The $M_d = 1.50$ nozzle operates at $M_j = 1.67$ and TTR = 1.00.

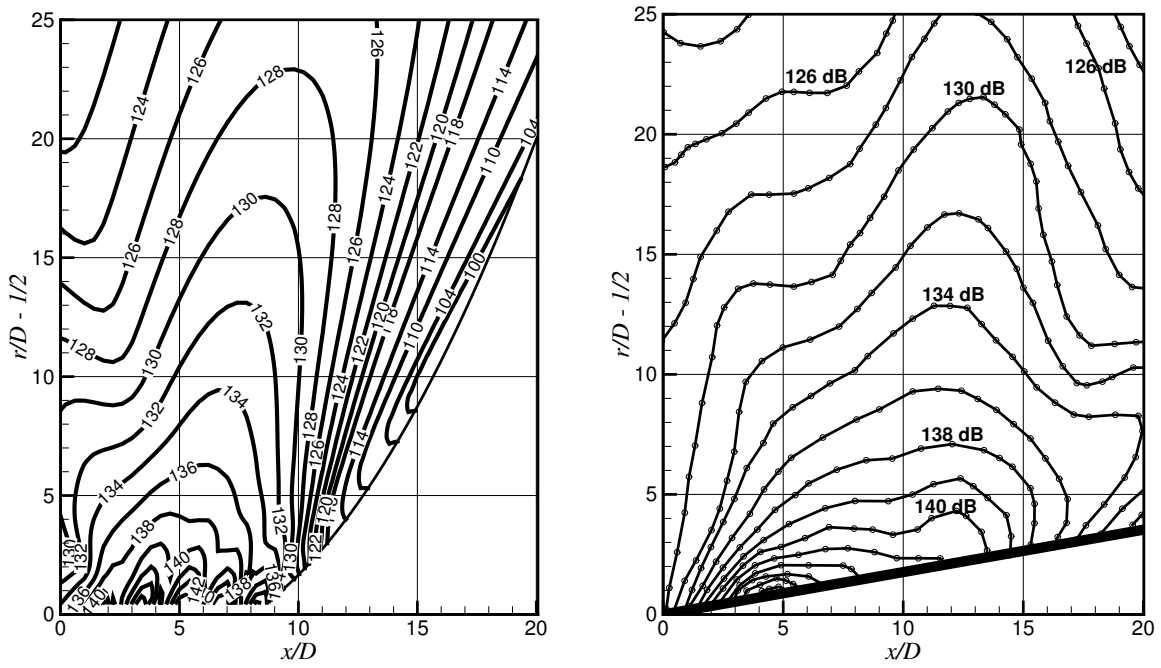

(a) BBSAN Prediction (b) Measurement

Figure 11. Near-field contours of SPL at 31.5 kHz. The $M_d = 1.50$ nozzle operates at $M_j = 1.67$ and TTR = 1.00.

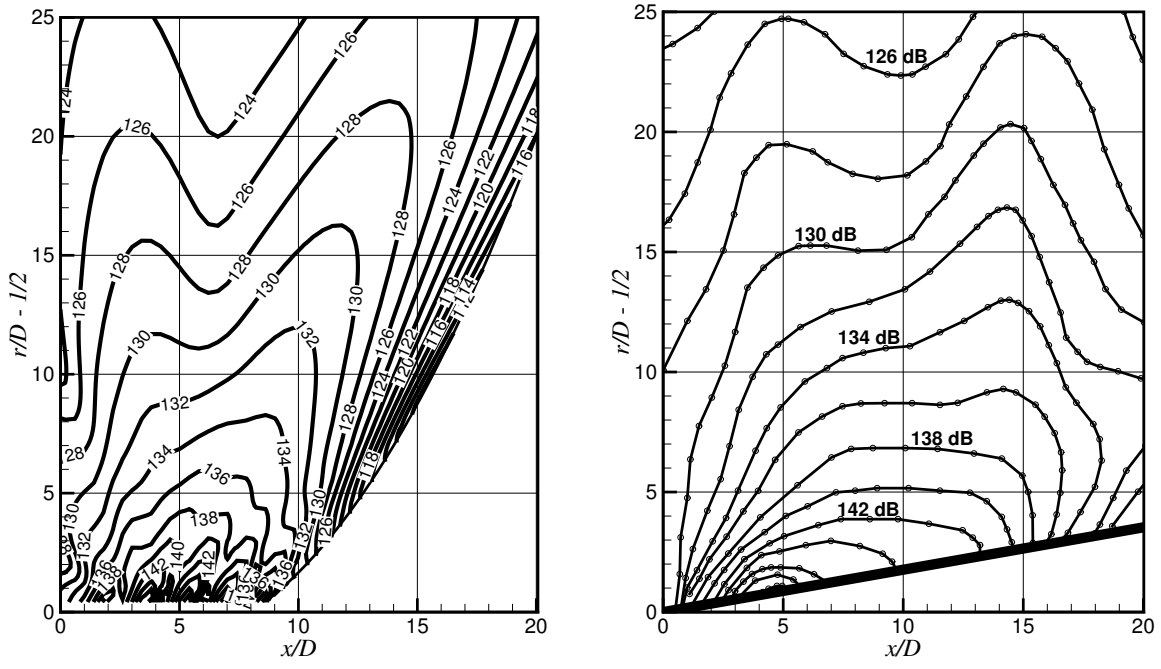

(a) BBSAN prediction (b) Measurement

Figure 12. Near-field contours of SPL at 40.0 kHz. The $M_d = 1.50$ nozzle operates at $M_j = 1.67$ and TTR = 1.00.

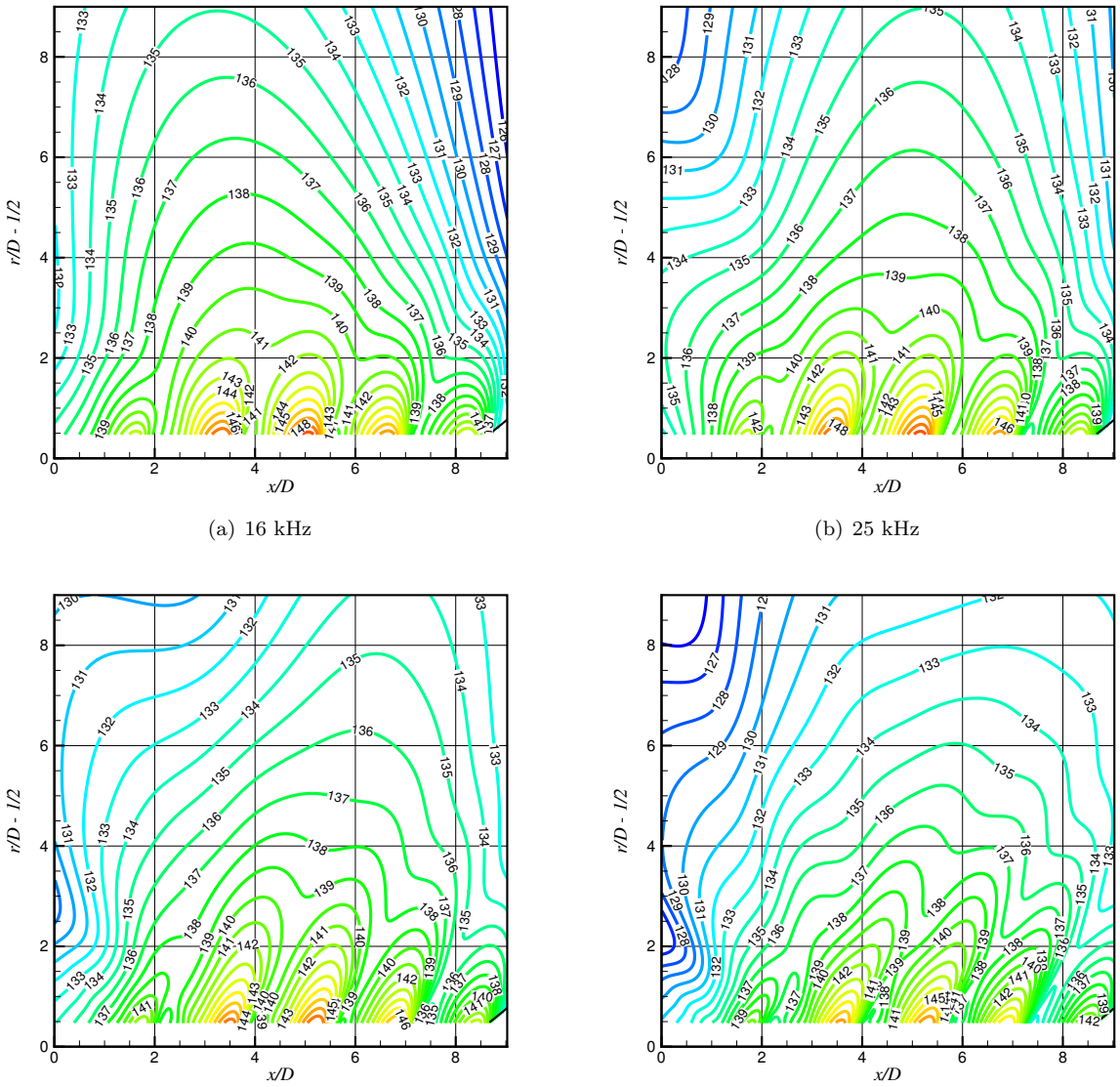

(a) 16 kHz

(b) 25 kHz

(c) 31.5 kHz

(d) 40 kHz

Figure 13. Predicted near-field contours of BBSAN intensity. The $M_d = 1.50$ nozzle operates at $M_j = 1.67$ and TTR = 1.00.

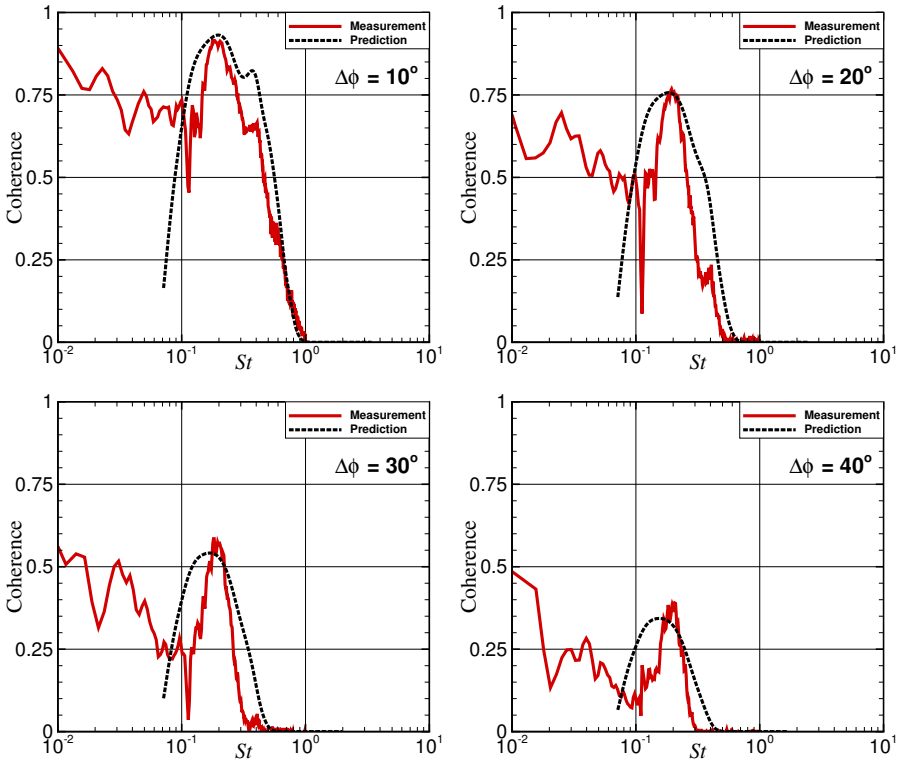

Figure 14. Predicted coherence compared with measurement for $M_d = 1.00$, $M_j = 1.57$, and TTR = 3.20. Comparisons are in the far-field at the sideline and $R/D = 100$. The observer microphone varies azimuthally.

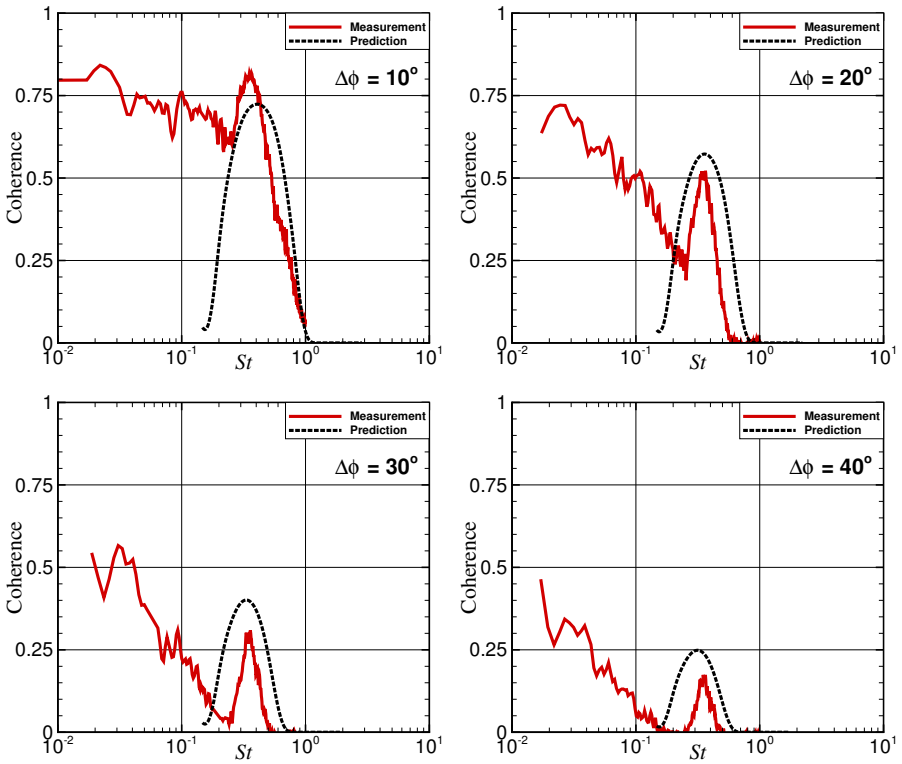

Figure 15. Predicted coherence compared with measurement for $M_d = 1.00$, $M_j = 1.24$, and TTR = 3.20. Comparisons are in the far-field at the sideline and $R/D = 100$. The observer microphone varies azimuthally.

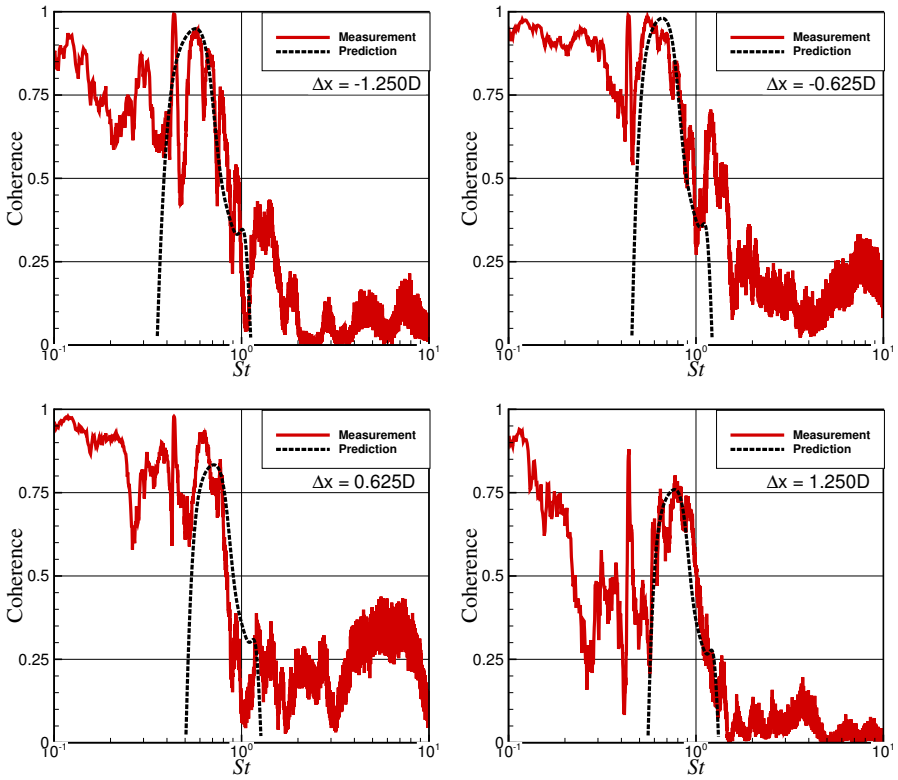

Figure 16. Predicted coherence compared with measurement for $M_d = 1.00$, $M_j = 1.22$, and TTR = 1.00. Comparisons are in the near-field at the sideline and $R/D = 4$. The observer microphone varies axially.

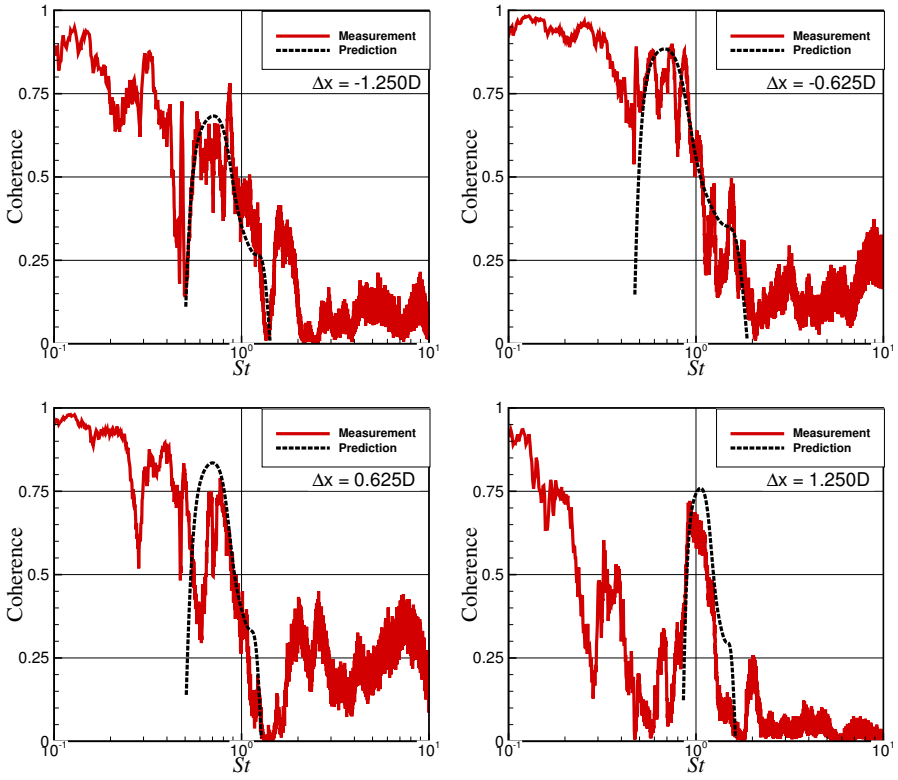

Figure 17. Predicted coherence compared with measurement for $M_d = 1.00$, $M_j = 1.16$, and TTR = 1.00. Comparisons are in the near-field at the sideline and $R/D = 4$. The observer microphone varies axially.

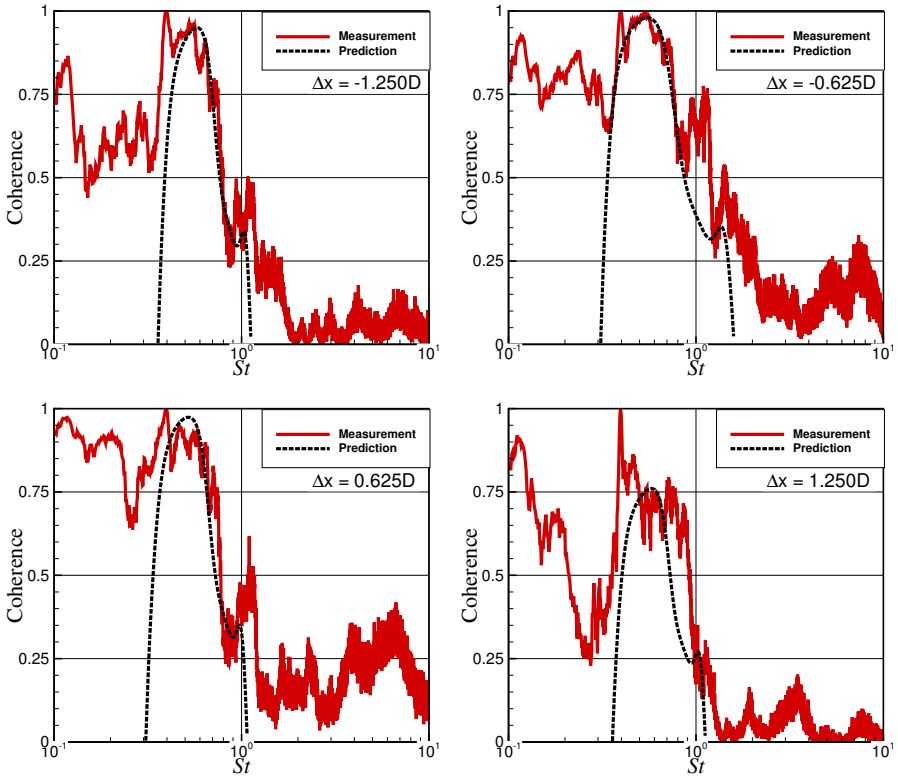

Figure 18. Predicted coherence compared with measurement for $M_d = 1.00$, $M_j = 1.28$, and TTR = 1.00. Comparisons are in the near-field at the sideline and $R/D = 4$. The observer microphone varies axially.